Controls of topographic Rossby wave properties and downslope transport in dense

- 2 overflows
- 3 Xianxian Han¹, Andrew L. Stewart², Dake Chen*1,3,4, Xiaohui Liu^{1,3}, Tao Lian^{1,3,4}
- 4 1 Southern Marine Science and Engineering Guangdong Laboratory (Zhuhai), China
- 5 2 Department of Atmospheric and Oceanic Sciences, University of California, Los
- 6 Angeles, California, USA
- 7 3 State Key Laboratory of Satellite Ocean Environment Dynamics, Second Institute of
- 8 Oceanography, Ministry of Natural Resources, China
- 9 4 School of Oceanography, Shanghai Jiaotong University, Shanghai, China
- 10 Corresponding to: <u>dchen@sio.org.cn</u>

Abstract

11

12

13

14

15

16

17

18

19

20

21

22

23

24

25

26

27

28

1

Antarctic Bottom Water is primarily formed via overflows of dense shelf water (DSW) around the Antarctic continental margins. The dynamics of these overflows therefore influence the global abyssal stratification and circulation. Previous studies indicate that dense overflows can be unstable, energizing Topographic Rossby Waves (TRW) over the continental slope. However, it remains unclear how the wavelength and frequency of the TRWs are related to the properties of the overflowing DSW and other environmental conditions, and how the TRW properties influence the downslope transport of DSW. This study uses idealized high-resolution numerical simulations to investigate the dynamics of overflow-forced TRWs and the associated downslope transport of DSW. It is shown that the propagation of TRWs is constrained by the geostrophic along-slope flow speed of the DSW and by the dynamics of linear plane waves, allowing the wavelength and frequency of the waves to be predicted a priori. The rate of downslope DSW transport depends nonmonotonically on the slope steepness: steep slopes approximately suppress TRW formation, resulting in steady, frictionally-dominated DSW descent. For slopes of intermediate steepness, the overflow becomes unstable and generates TRWs, accompanied by interfacial form stresses that drive DSW downslope relatively rapidly. For gentle slopes, the TRWs lead to the formation of coherent eddies that inhibit downslope DSW transport. These

findings may explain the variable properties of TRWs observed in oceanic overflows, and imply that the rate at which DSW descends to the abyssal ocean depends sensitively on the manifestation of TRWs and/or nonlinear eddies over the continental slope.

1. Introduction

The formation of Antarctic Bottom Water (AABW) ventilates abyssal ocean and plays a key role in global overturning circulation and climate (Talley, 2013). AABW sources from the descent of dense shelf water (DSW), which forms through sea ice growth and ocean/ice-shelf interactions around Antarctic coast. Specifically, DSW primarily forms over the Weddell Sea (Foldvik et al., 2004), the Ross Sea (Gordon et al., 2009), the Adelie coast (Williams et al., 2008), and Prydz Bay (Oshima et al., 2013). With sufficient large density, DSW can overflow across the shelf break and descend down to deep ocean, which has been widely observed over the global ocean (Ivanov et al., 2004; Legg et al., 2009). The mechanism via which DSW descends the slope could additionally influence the rate at which lighter waters are entrained into the DSW, and thus the properties and flux of AABW (Legg et al. 2009).

Theoretically, under the influence of the Earth's rotation, the overflows in the southern hemisphere should turn to the left to flow approximately along isobaths over a period comparable to the inertial time scale, then descend gradually via the action of bottom Ekman transport. Killworth (2001) predicts the descent rate of DSW induced by bottom Ekman transport to be 1:400, i.e., the dense water descends 1km vertically, while advancing 400km in the along-slope direction. However, in-situ observations show that dense overflows can reach the deep ocean over much shorter along-slope distances (Gordon et al., 2009; Foldvik et al., 2004; Oshima et al., 2013). This indicates that additional dynamical mechanisms must break the geostrophic constraint to accelerate the descent of the DSW.

One way in which observed outflows of dense water deviates from this theoretical conception is that they may exhibit pronounced variability associated with the genesis and propagation of Topographic Rossby Waves (TRWs; Pedlosky, 1987; Marques et al., 2014). For example, TRWs forced by dense overflows have been observed in the Weddell Sea (Jensen et al., 2013), in Prydz Bay (Nakayama et al., 2014), across the Denmark Strait

(Hopkins et al., 2019) and in the Faroe Bank Channel (Darelius et al., 2015). In contrast, the Ross Sea and Adelie coast overflows, where the continental slopes are very steep, exhibit no significant oscillations other than tides (Gordon et al., 2009; Williams et al., 2010). This implies that some combination of the local environment and the dynamics of the overflow dictate the presence or absence of TRWs. Results from numerical modeling studies are consistent with this implication, and further show that the properties of the TRWs are coupled to the dense overflow (Jiang and Garwood, 1996; Han et al., 2022). However, it remains unclear what dynamics select the specific wavelength and frequency of the TRWs that manifest in a given DSW overflow.

Previous studies also suggest that genesis of TRWs in DSW overflows may play a key role in facilitating the downslope flow. For example, the growth of baroclinic waves in the overflowing DSW may lead to genesis of mesoscale eddies, which have been identified as a conveyor of DSW along or down continental slopes in various modeling studies (Gawarkiewicz and Chapman, 1995; Jiang and Garwood, 1995; Tanaka and Akitomo, 2001; Matsumura and Hasumi, 2010; Nakayama et al., 2014; Stewart and Thompson, 2016). For a dynamical description of this eddy genesis, we draw on the theory of Swaters (1991), which has been widely used to interpret the dynamics of baroclinic instability in overflows (Jiang and Garwood, 1995; Tanaka and Akitomo, 2001; Guo et al., 2014; Han et al., 2022). In this theory, the instability takes the form of growing TRWs in the overlying water that are geostrophically coupled via the pressure field to the DSW overflow. Whether these TRWs grow sufficiently large in amplitude to form nonlinear eddies depends on the local environmental conditions, especially the steepness of the continental slope (Jiang and Garwood 1996; Han et al. 2022).

In contrast to baroclinic instability over a flat sea floor, in which available potential energy is released via slumping of isopycnals (Pedlosky, 1987), the instability of the dense overflow releases potential energy by migrating deeper down the continental slope (Reszka et al., 2002). Thus, from an energetic perspective, genesis of TRWs necessitates downslope flow of DSW because it provides the energy required for them to grow; this holds regardless of whether those TRWs grow into nonlinear eddies. However, it remains unclear

how variations in the behavior of TRWs, for example due to variations in environmental conditions, translate to changes in the downslope flow of DSW.

In this paper, we use an idealized high-resolution numerical model to investigate the properties of overflow-forced TRWs and the associated downslope transport of DSW, across a range of regimes of overflow variability. In section 2, we formulate an idealized model to allow exploration of a wide range overflow dynamical regimes. In section 3, we show that the geostrophic along-slope flow speed of the DSW and the intrinsic dynamics of TRWs determine the wavelength and frequency of TRWs. In Section 4 we discuss the dynamics of TRW-mediated downslope transport of DSW, and quantify the rates of downslope DSW transport across steady, wavy and eddying overflow regimes. In Section 5 we summarize and discuss our findings.

2. Model configuration

The model we use is Regional Ocean Modeling System (ROMS), which has been widely used to investigate oceanic flows over steep slopes (Shchepetkin and McWilliams, 2003; Ilicak et al., 2011). A detailed description of the model setup is given by Han et al. (2022), so here we only describe salient features of the model in the interest of a self-contained presentation.

To investigate the dynamics across a range of different overflow regimes, we use a highly idealized bathymetric geometry, as shown in Fig. 1a. A northward-flowing intrusion of DSW with density anomaly of $\Delta\rho \sim 0.2~kg/m^3$ (Gordon et al., 2009) is imposed in a trough on the continental shelf, from which it overflows and descends the continental slope. To ensure that the structure of the inflow changes as little as possible within the trough, we follow the prescription of Legg et al., (2006). The dense inflow flux is about 0.2Sv, which is relatively small compared to the estimated DSW flux \sim 0.8Sv in the Ross Sea (Gordon et al., 2009) and 1.6±0.5Sv in the Weddell Sea (Foldvik et al., 2004), but not unreasonable considering that the model is a highly idealized representation of dense overflows. To track the dense overflow, we inject passive tracer with initial concentration $\tau = 1$ in the dense inflowing water. All the simulations start from rest, and there is no other forcing except the dense inflow: the eastern, western and northern boundaries all use radiation conditions.

The horizontal grid spacing ranges from 0.5km near the trough region, which is sufficient to resolve mesoscale eddies (St Laurent et al. 2013; Stewart and Thompson, 2015), to ~2km at the open boundaries. There are 60 topography-following levels in the vertical direction, with finer vertical grid spacing close to the sea floor (~5m over the upper slope). The initial stratification is adapted from *in situ* observations in the Ross Sea (Station 47, Gordon et al., 2009), as shown in Fig. 1(b-d). We use a constant Coriolis parameter $f = -1.38 \times 10^{-4}$ (~72°S) throughout the model domain. Vertical viscosity and mixing are parameterized via the Mellor-Yamada level 2.5 turbulence closure scheme (Mellor and Yamada, 1982). The benthic stress is parameterized as a quadratic drag with constant drag coefficient of Cd=0.003. The horizontal mixing of momentum and tracers are parameterized via Laplacian operators, with the same and constant coefficients for lateral viscosity and diffusivity (5 m^2/s).



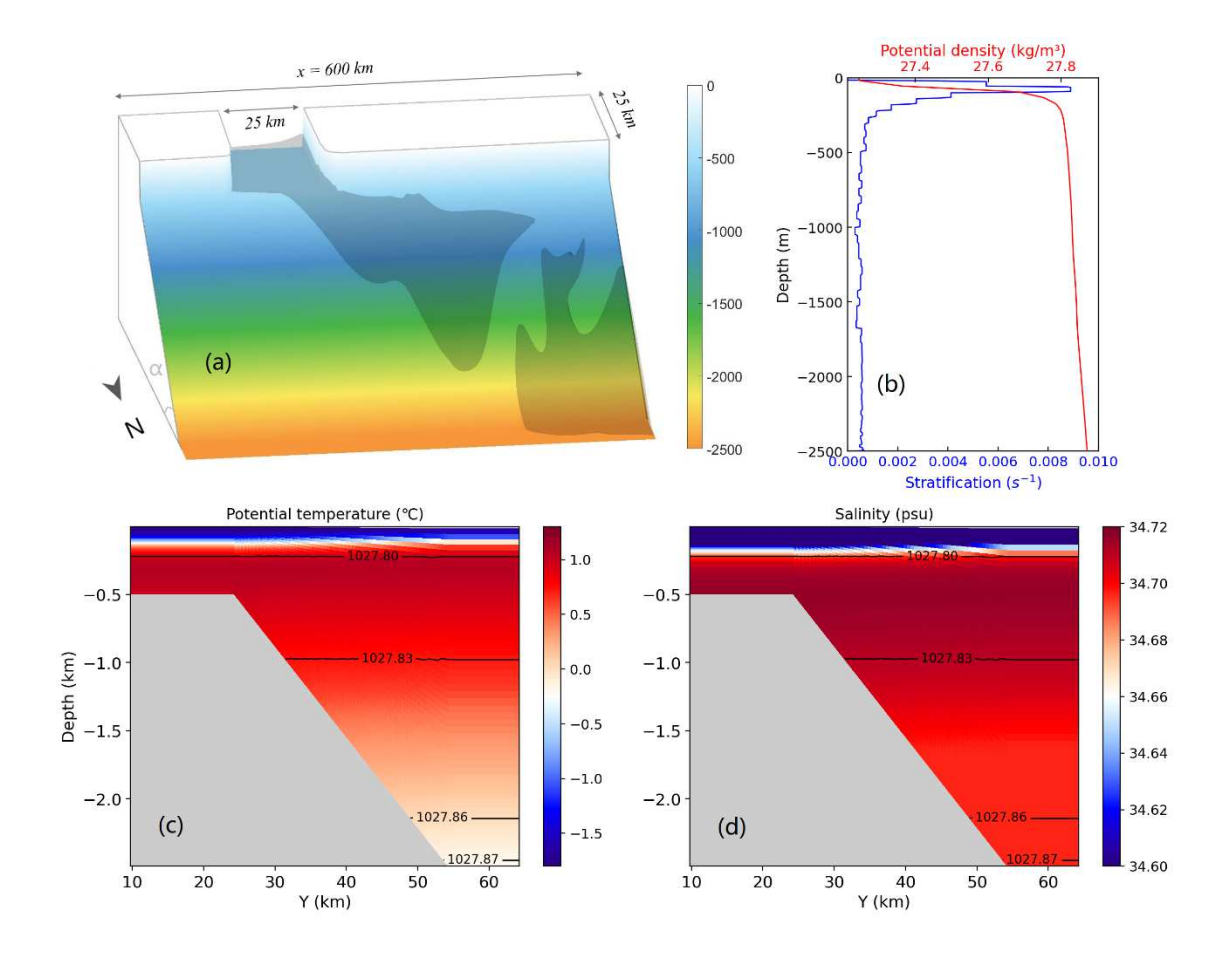


Figure 1. (a) Schematic showing the model bathymetry, with slope steepness $s = \tan \alpha$. Grey shading shows a representative snapshot of the overflow dense water thickness. (b) Initial potential density (with 1000 kg/m³ subtracted, referenced to surface) and buoyancy frequency profile. The green line approximately indicates the base of the pycnocline (~150m). (c-d) Initial potential temperature and salinity. Black contours show potential density referenced to the surface.

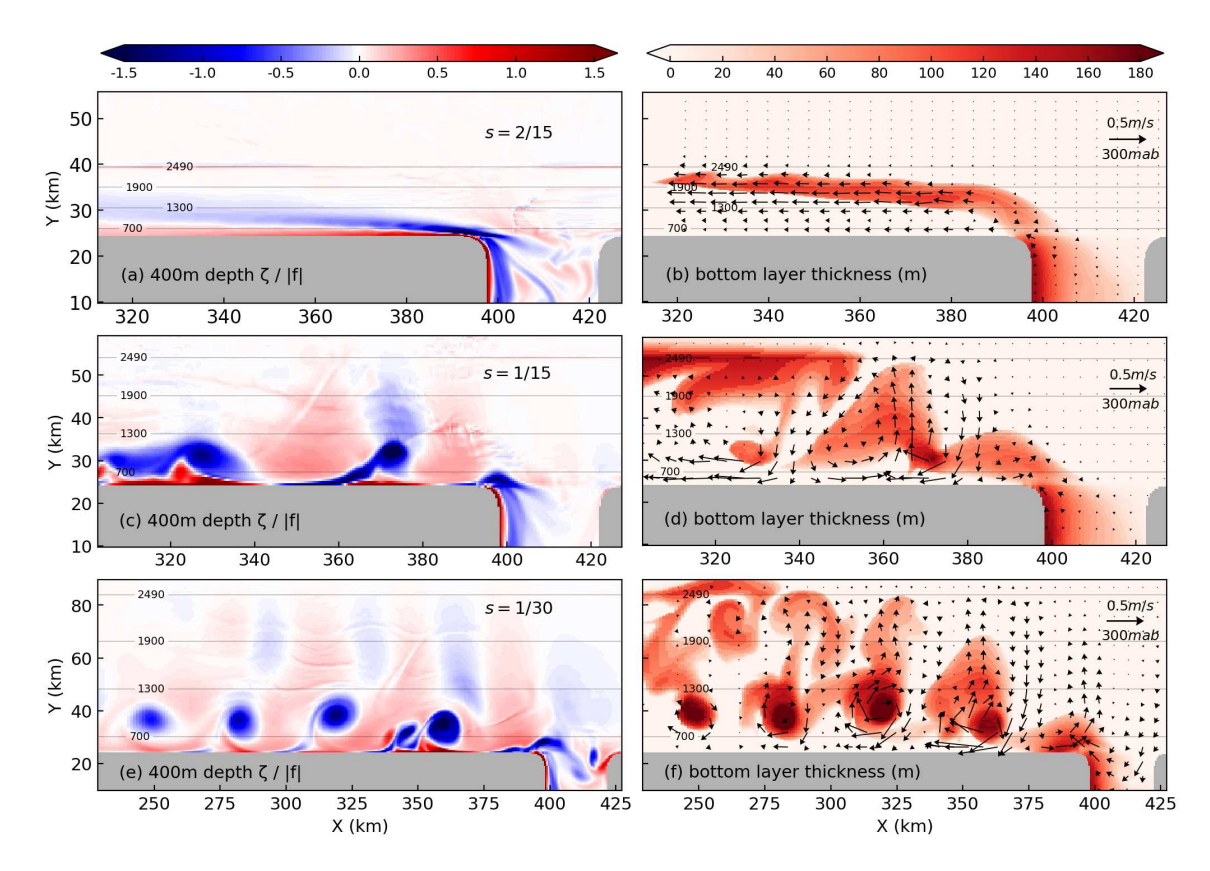
Previous theoretical analysis (Swaters, 1991) and sensitivity experiments (Jiang and Garwood 1996; Han et al., 2022) indicate that the slope steepness strongly influences the dynamics of the overflow. Therefore, we conduct a series of experiments with different slope steepnesses to span a range of different overflow regimes. For the experiment with the steepest slope (s = 2/15), we use near-trough horizontal grid spacings of both 250m and 500m to ensure that the solution is not influenced by pressure errors associated with the terrain-following coordinates. The results are very similar, so here we present diagnostics from the simulation with a grid spacing of 250m. We summarize the key model parameters in table 1. All simulations are integrated to steady state, as indicated by steady oscillations in the model state variables, which typically occurs after \sim 30 days. We then analyze the last \sim 10 days (\sim 5 TRW periods) of integration using hourly-averaged model output.

Table 1. List of parameters used in our simulations.

Parameter	Description	Value
S	Slope steepness	1/50-2/15
f	Coriolis parameter	$-1.38 \times 10^{-4} \text{ s}^{-1}$
N	Stratification below pycnocline	$\sim 6 \times 10^{-4} \text{ s}^{-2}$
A_h	Horizontal viscosity	$5 \text{ m}^2 \text{s}^{-1}$
K_h	Horizontal diffusivity	$5 \text{ m}^2 \text{s}^{-1}$
Δχ, Δy	Horizontal grid spacing	0.25-2 km
Δz	Vertical grid spacing	4-30 m
D	Maximum depth	2500 m
C_d	Bottom friction coefficient	$3 \times 10^{-3} \text{ m} \cdot \text{s}^{-1}$
Δρ	Density anomaly of dense inflow	$0.2 \ kg \ /m^3$

Fig. 2 shows the phenomenology of three representative experiments with different slope steepnesses. These slopes correspond approximately to the steepnesses of the Ross Sea continental slope (s = 2/15), and of the upper continental slope (s = 1/15) and middle continental slope (s = 1/30) of the southern Weddell Sea. We will henceforth refer to these specific simulations as the "steep slope", "moderate slope" and "small slope" cases,

respectively. Since the strength of waves vary substantially in different experiments, we take the ratio of eddy kinetic energy and mean kinetic energy in the wave region (see section 3) as a criterion to define the absence/presence of waves. If the ratio is smaller than 0.1, we define it as having "no waves". The steep slope experiment shows no waves, with the dense overflows taking the form of a steady along-slope geostrophic flow after its initial geostrophic adjustment (Fig. 2(a-b)). In contrast, there are visible TRWs in moderate slope experiment, and the dense overflows exhibits downslope transport aligned with the offshore wave circulations, as visualized by the black arrows in Fig. 2(c-d). Associated with the negative phase of these waves are patches of negative vorticity, which have been identified to be coherent eddies via the deployment of Lagrangian floats (see Han et al., 2022). The formation of eddies is due to the feedback of the waves on the outflow at the trough mouth, which is why they have the same frequency as the waves (Han et al., 2022). When the slope is smaller, the phenomenology is similar to the moderate slope experiment. A distinguishing feature of this experiment is that there are isolated bottom eddies along the upper slope (Fig. 2f). In the following sections, we will separately analyze the overflowforced TRWs and the associated downslope transport of DSW.



155

156

157

158

159

160

161

162

163

164

165

166

167

168

169

Figure 2. Snapshot of three cases with different slope steepnesses. (a) Normalized relative vorticity $(\zeta/|f|)$ at 400m depth with slope steepness s = 2/15. (b) The corresponding bottom dense water thickness ($\rho \ge 1027.88 \, kg/m^3$, referenced to surface). Arrows indicate flow velocity at 300 mab (meters above bottom), and contours indicate bathymetric depths in meters; (c-d) Same as (a-b), but for the experiment with slope steepness s = 1/15. (e-f) Same as (a-b), but for the experiment with slope steepness s = 1/30. Note the different axis ranges for different experiments.

3. Wavelength and frequency of overflow-forced topographic Rossby waves

As noted in section 1, TRWs have been observed in several dense overflows in nature (Jensen et al., 2013; Nakayama et al., 2014; Hopkins et al., 2019; Darelius et al., 2015), and have been attributed to instability of the overflow in various modeling studies (Jiang and Garwood 1996; Tanaka and Akitomo, 2001; Guo et al., 2014; Han et al., 2022). Linear baroclinic instability theory provides some insight into the genesis of these TRWs (Swaters, 1991; Jungclaus et al., 2001; Guo et al., 2014): for example, the overflow is stabilized, and thus TRWs are suppressed, when the width of the continental slope falls below the minimum unstable wavelength predicted by the theory (Han et al. 2022). However, in parameter regimes in which TRWs are present, their wavelength and frequency are better predicted by linear plane TRW theory, rather than linear baroclinic instability theory (Marques et al. 2014; Han et al. 2022). Thus there is yet no explanation for the specific wavelength and frequency of the overflow-forced TRWs. In this section, we posit that the TRW wavelength and frequency is selected by a coincidence between the TRW propagation speed and the geostrophically-constrained along-slope speed of the overflow, and test this relationship using our model simulations.

The theoretical ideas that underpin the propagation of the dense overflows and TRWs are summarized schematically in Fig. 3. We consider the dynamics associated with an isolated "pulse" of the dense overflow, resulting from baroclinic instability. Compression and stretching of the overlying waters induce the generation of relative vorticity (ζ) via conservation of potential vorticity, leading to propagating of TRWs (Swaters 1991; Swaters and Flierl, 1991). The westward propagation of these TRWs is accurately captured by linear plane wave theory (Marques et al. 2014; Han et al. 2022), which predicts a along-slope phase speed c_p given the TRW wavelength. This yields a first constraint on the properties of the TRWs.

A second constraint on the propagation is provided by the geostrophic dynamics of isolated dense "pulses" over sloping topography. Based solely on the assumption of geostrophy and that the dense layer incrops into the upper and lower continental slope, it may be shown that such dense pulses should translate westward at the "Nof" speed (Nof, 1983),

$$U_N = \frac{g's}{f}.$$
 (1)

Here $g' = g\Delta\rho/\rho$ is the reduced gravity and s is the topographic slope steepness. Thus in order for the vorticity anomalies that comprise the TRW in the overlying water to remain collocated with the pulses of dense overflow water, the TRW propagation speed must match the Nof speed. We note that this coincidence of the TRW propagation speed and the theoretical Nof speed may only be approximate: the Nof speed assumes negligible bottom friction and zero flow in the overlying waters (Nof, 1983), so some departures of the diagnosed westward speed (U_d) from Eq. (1) are to be expected.

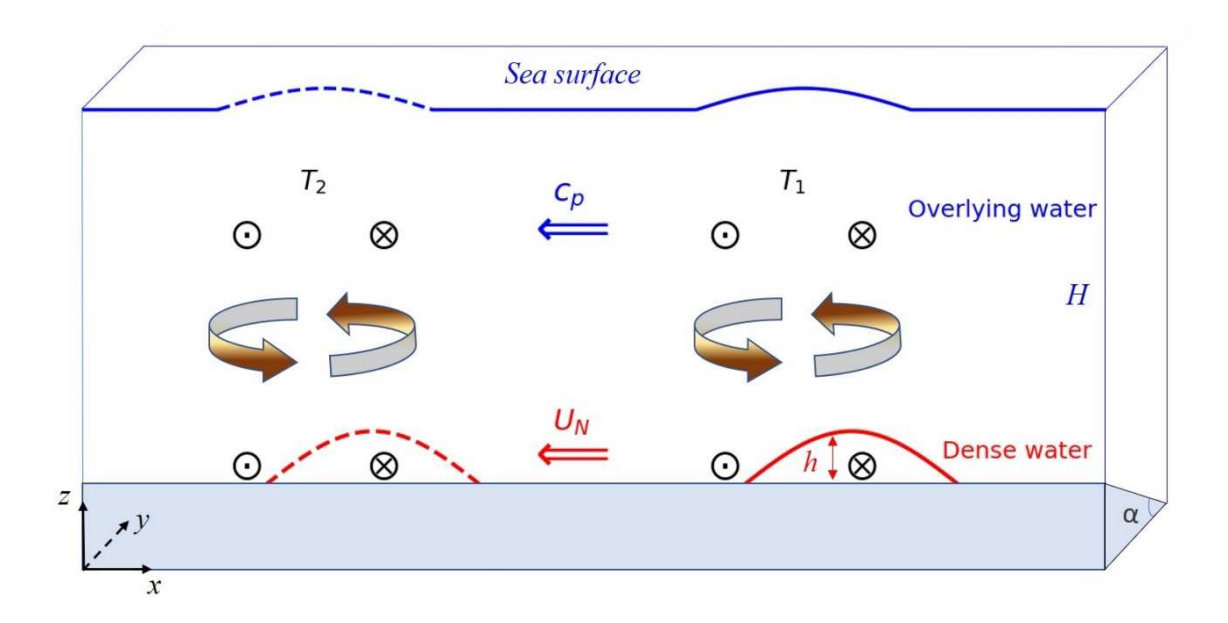


Figure 3. Schematic showing the interactions between dense overflow and overlying water over sloping topography. c_p and U_N indicate phase speed of waves and the intrinsic Nof speed of dense overflows respectively. They propagate along-slope at the same speed, but remain out of phase, as required to

release potential energy from the dense overflows¹. The heads and tails of arrows indicate upslope and downslope flow respectively, which are induced by the squeezing of overlying water as dense water pass by. T_1 and T_2 indicate two snapshots at different times, implying a westward propagation.

To test the relevance of these theories in our simulations, we compare c_n with U_N and U_d respectively, and normalize the differences by the absolute value of c_p . To diagnose the properties of the simulated waves, we extract meridional velocity from an along-slope section crossing the red star in Fig. 4, where the waves have reached a relatively mature state. Then we obtain the zonal wavenumber k by computing the time-averaged distance between the nearest wave peak and trough of the red star. This approach to calculating the wavenumber could be improved by spectral analysis (Marques et al., 2014), but has been previously shown to produce close agreement with linear TRW theory (Han et al., 2022). The frequency (ω) of waves is estimated via Fourier spectral analysis. We then compute the TRW phase speed $c_p = \omega/k$. To calculate the Nof speed U_N , we compute $\Delta \rho$ as the difference between dense overflow layer ($\rho \ge 1027.88 \, kg/m^3$) vertical averaged density and the density in the 20^{th} σ layer, which ranges from \sim 200mab near the shelf break to \sim 1000mab in deep ocean. We diagnose U_d as the vertically- and time- averaged zonal flow speed in dense overflow layer, i.e. the thickness-weighted average of the zonal velocity (Young 2012). Fig. 4 shows the results for our moderate slope and small slope experiments. Overall, the differences between c_p and U_N are relatively small if we exclude the upstream region $(x \ge 380 \text{ km})$, where the dense overflow is still under geostrophic adjustment process (Fig. 4(a, c)). However, the differences between c_p and U_d are larger, especially on the upper and lower slope, with opposite sign (Fig. 4(b, d)).

221

222

223

224

225

226

227

228

229

230

231

232

233

234

235

236

237

238

239

240

241

⁻

¹ There must be some misalignment between the vorticity anomalies in the overlying waters and dense water pulses to release potential energy of DSW, just as the classical Phillips baroclinic instability theory (Cushman-Roisin and Beckers, 2009).

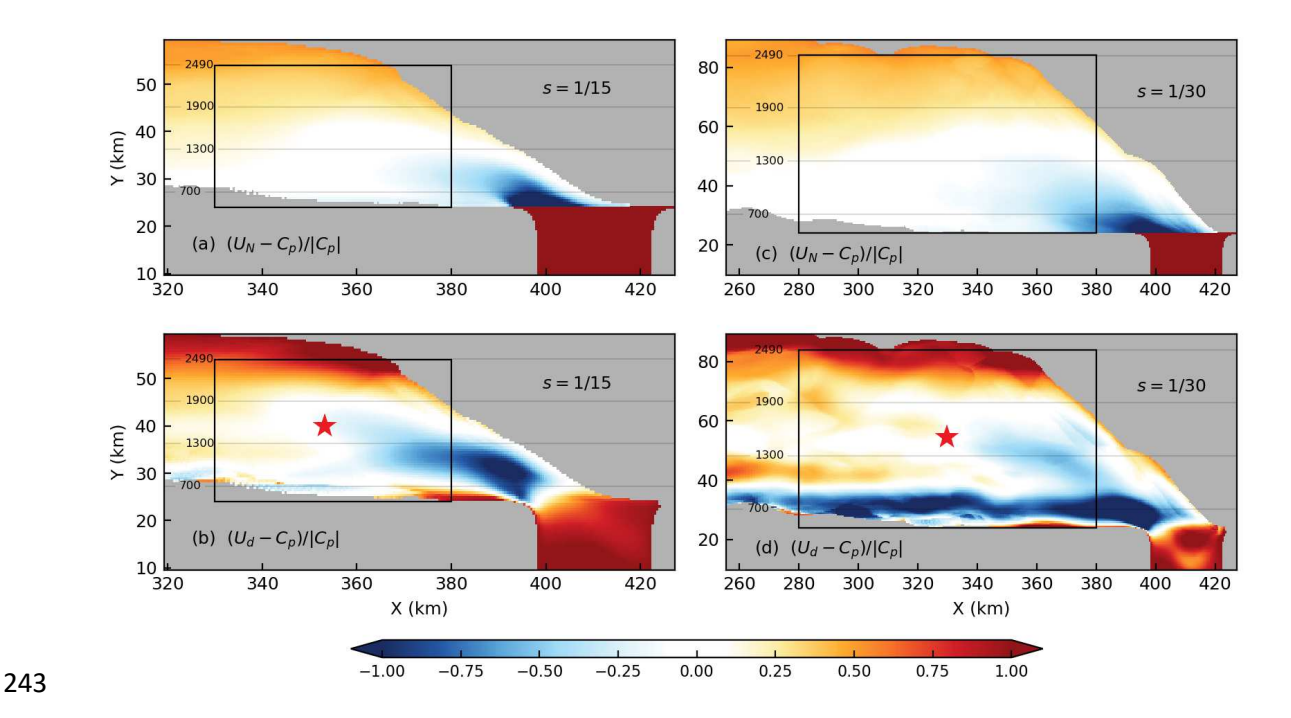


Figure 4. The difference between the diagnosed phase speed of the topographic Rossby waves and the westward flow speed of the dense overflow ($\rho \geq 1027.88 \ kg/m^3$), normalized by the phase speed. The black rectangles indicate the areas used to compute averages in Fig. 5. (a) The time-averaged difference between phase speed (c_p) and Nof speed (U_N) with topographic slope s=1/15. (b) The time averaged difference between phase speed (c_p) and diagnosed overflow speed (U_d) with topographic slope s=1/15. (c-d) As panels (a-b), but with topographic slope s=1/30. The red stars indicate the location used to diagnose the waves' length, frequency and phase speed.

In Fig. 5 we provide a spatially- and temporally-averaged quantification of the agreement between c_p , U_N and U_d . We perform the spatial average over the regions in which the waves are most active, indicated by the black rectangles in Fig. 4. Because the amplitude of the TRWs diminishes with distance downstream (Fig. 2), the zonal length of the wave regions ranges from 1 to 3 wavelengths. However, our results are not sensitive to the definition of spatial range of the wave region, due to the generally small difference between the flow speed and wave phase speed (Fig. 4). In Fig. 5a, we show the results of all our experiments with varying slope steepnesses: in each simulation we diagnose the wave properties in the center of the corresponding analysis box. Overall, the diagnosed c_p , U_N and U_d are very close to each other, especially for the experiments with smaller topographic slopes ($s \le 0.08$). However, for experiments with steeper slopes (s > 0.08),

 c_p diverges somewhat from U_N and U_d . We can interpret this trend with the aid of the interaction parameter (μ) , defined by Swaters (1991) as

$$\mu = \frac{h}{sR}, \qquad (2)$$

where h, s and R represent the dense overflow thickness, slope steepness and Rossby deformation radius, respectively. This parameter expresses the interaction strength between the dense overflow and the overlying water, with larger value representing stronger interaction. Under the conditions of constant dense inflow flux and overlying stratifications in our simulations, the interaction parameter decreases as the slope steepness increases, leading to weaker interactions. Fig. 5b shows the dependence of c_p , U_N and U_d on the interaction parameter: this plot shows that the divergence of c_p from U_N and U_d occurs for smaller values of the interaction parameter ($\mu \le 0.15$), suggesting that the coupling between the dense "pulses" of overflow waters and the overlying TRWs breaks down in this parameter regime. The larger departures between wave phase speed and overflow speed for steep slopes may be due to constraint that baroclinic waves are inhibited from growing when their wavelength is smaller than the width of the continental slope (Han et al., 2022); this is supported by diagnosed wavelength being smaller than the theoretically-predicted wavelength in the steep slope experiment (s = 2/15) (Fig. 6).

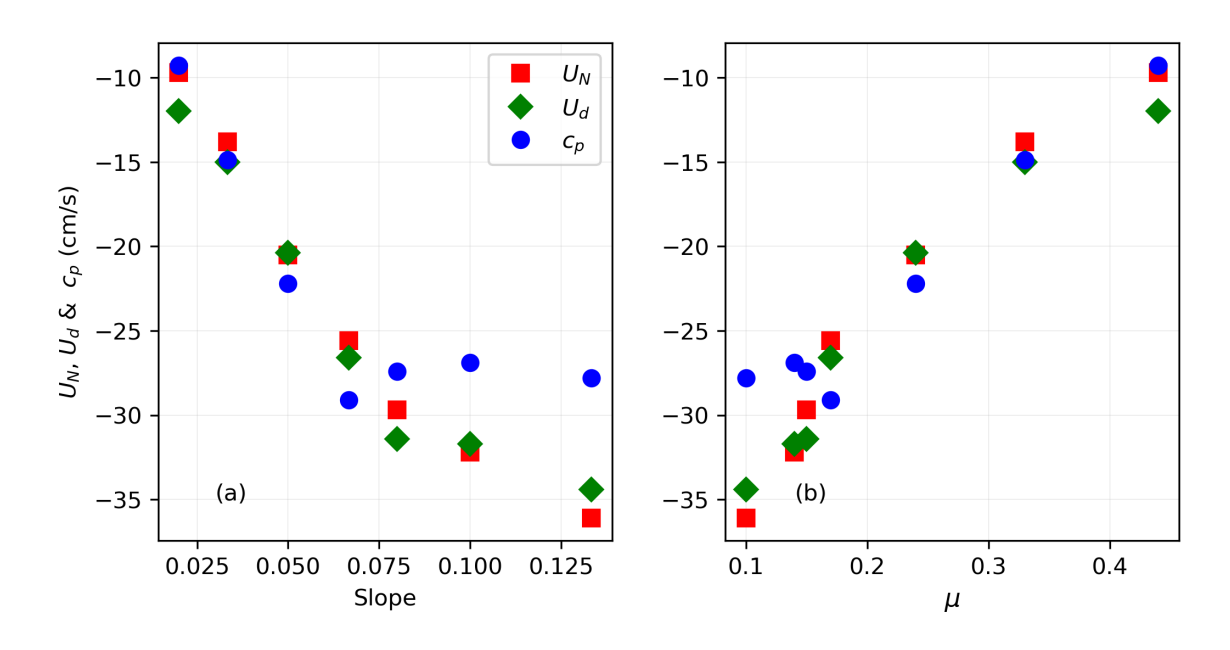


Figure 5. Spatially and temporally averaged c_p , U_N and U_d in the regions of elevated wave activity, which are identified by the black rectangles in Fig. 4. (a) Dependence on slope steepness (s). (b) Dependence on interaction parameter (μ) .

The above analysis indicates that the propagation speed of the dense overflow (i.e. approximately the Nof speed) sets the phase speed of overlying TRWs. We can therefore predict the wavelength and frequency by considering the dynamics of linear plane waves (Marques et al. 2014; Han et al. 2022). For simplicity, we assume a constant stratification N_0 (6 × 10⁻⁴ s^{-2}), and treat the pycnocline ($z \sim$ -150m) as a rigid lid. Then the dispersion relationship for linear plane TRWs (Pedlosky, 1987) can be expressed as

$$\omega = \frac{N_0 sk}{K \tanh\left(\frac{N_0 K}{f_0}H\right)},$$
 (3)

290 where *H* is the water column thickness (below 150m depth) and $K = \sqrt{k^2 + l^2}$ is the absolute wavenumber. The along-slope phase speed can be expressed as

$$c_p = \frac{\omega}{k} = \frac{N_0 s}{K \tanh\left(\frac{N_0 K}{f_0}H\right)},\tag{4}$$

Although TRW can propagate their phase across topography (Rhines, 1970), which is supported in observations both in the deep ocean at mid-latitudes (Pickart and Watts, 1990) and dynamically wide channels at polar latitudes (Muenchow et al., 2020), the phase propagation of TRW in our idealized experiments is almost along-slope (see Appendix). Henceforth we assume that the waves are directed westward, i.e. l = 0 and K = k. Fig. 6 shows the dispersive curves of 6 experiments with varying slope steepnesses, with the colored diamonds representing the diagnosed phase speed and frequency for different experiments. We can see that the diagnosed wave properties in each experiment are very close to the corresponding dispersion curve for linear TRWs, which indicates that the shallow-water waves in our simulations are TRWs.

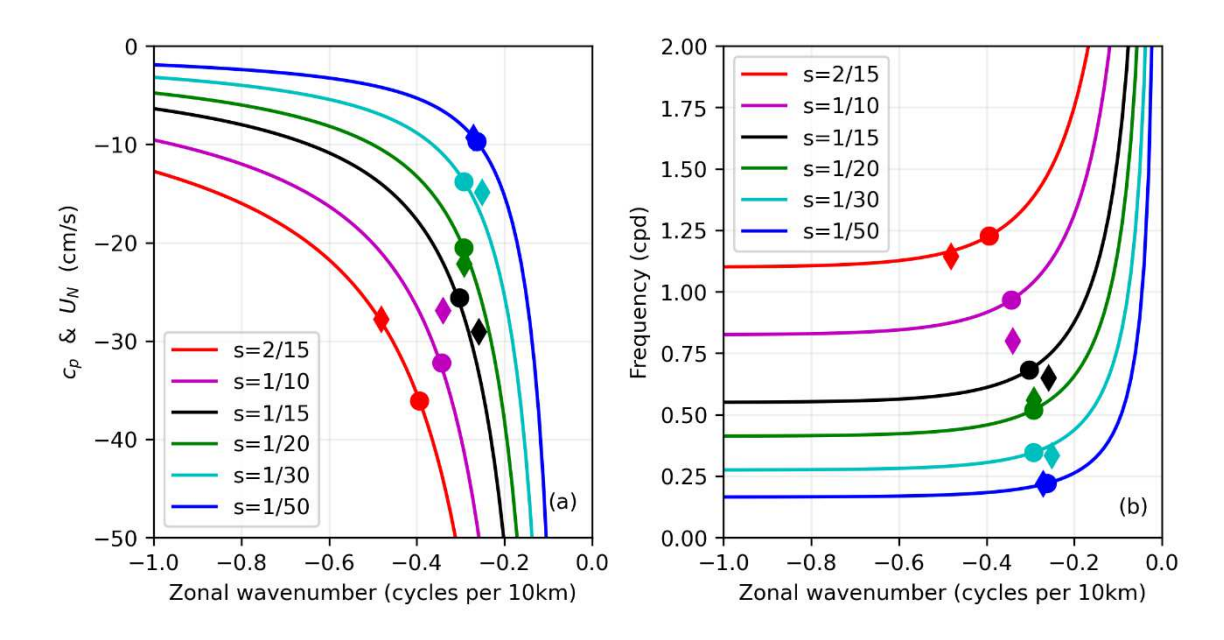


Figure 6. Dispersive curves of linear plane TRWs with varying slope steepness. The diamonds with the same color as the dispersive curves indicate properties diagnosed from the corresponding model simulations, while dots indicate the results predicted by assuming that the wave phase speed matches the Nof speed (Equation (5)). (a) Phase speed of TRWs versus zonal wavenumber. (b) Frequency of TRWs versus zonal wavenumber.

We now predict the wavelength and frequency of the TRWs by equating the theoretical phase speed with the Nof speed, i.e.

$$c_p = \frac{N_0 s}{K \tanh\left(\frac{N_0 K}{f_0}H\right)} \approx \frac{g' s}{f}.$$
 (5)

Note that because the phase speed of the TRWs is related to the wavelength via Eq. (4), we can use Eq. (5) to predict the TRW wavelength, and then use Eq. (3) to predict the frequency. The colored dots in Fig. 6a show the wavelength estimated by Eq. (5) for different experiments, and the corresponding frequencies are shown in Fig. 6b. The results show that the overflow-derived (dots) and the diagnosed (diamonds) wave properties are very close to each other, which supports our hypothesis that the wavelength and frequency of the TRWs are determined by the Nof speed of the dense overflow and the intrinsic dynamics of TRWs.

This method can be extrapolated to estimate the properties of overflow-forced TRWs in nature. The oceanic overflow speeds (U_N) observed over continental slope are typically around 0.5m/s, because stronger flows tend to develop shear instabilities that entrain overlying waters (Legg et al., 2009). We assume that the wavelength cannot be smaller than 10km for our assumption of geostrophy to apply (Swaters, 1991; Han et al., 2022). Given these limitations, the estimated wavelength is 10-100km and the period is in the range of 1 to 10 days over the range of topographic slopes found in oceanic overflows $(1/50 \le s \le 2/15)$. This range is consistent with the baroclinic instability theory (Swaters, 1991), other numerical experiments (Marques et al., 2014; Nakayama et al., 2014) and observations (Ohshima et al., 2013; Darelius et al., 2009; Jensen et al., 2013).

As shown in Equation (3) and (5), in addition to the overflow speed and slope steepness, the overflow-derived wavelength and frequency of TRWs also depend on the density stratification (N), the Coriolis parameter (f) and the water column thickness. Although the dispersive curve will shift according to local environmental conditions, this method provides a straightforward and general estimate of wavelength and frequency of overflow-forced TRWs. For example, based on this method, stronger overlying stratification produces a shorter TRW wavelength for a constant overflow speed (not shown), which is consistent with linear baroclinic instability theory that incorporates a continuously stratified upper layer (Reszka et al., 2002).

4. TRW-mediated downslope transport of dense overflows

As noted in section 1, the variability of the overflow varies substantially with the steepness of the continental slope, or equivalently with the magnitude of the interaction parameter. Steep slopes entirely suppress TRWs, while gentler slopes permit more energetic TRWs that may form coherent eddies (Fig. 2). In this section, we will investigate the mechanisms via which dense water is driven to descend the continental slope across these steady, wavy and eddying regimes, and the resulting variations in the descent rate.

4.1 Drivers of down-slope flow

To quantify the mechanisms responsible for driving the down-slope flow, we use the depth-integrated isopycnal momentum budget, which has been widely used to interpret drivers of meridional transport across the Southern Ocean (Mazloff et al., 2013; Howard et al., 2015; Masich et al., 2018). The momentum equation per unit volume in zonal direction is

352
$$\frac{\partial u}{\partial t} + \boldsymbol{u} \cdot \nabla u - f v = -\frac{1}{\rho_0} \frac{\partial p}{\partial x} + \frac{1}{\rho_0} \frac{\partial \tau^x}{\partial z}, \quad (6)$$

where $\mathbf{u} = (u, v, w)$, p is pressure and τ^x is zonal friction. Then we integrate vertically 353 from sea floor to the upper interface of the dense water layer, which remains to be defined. 354 In the initially-imposed model stratification, the maximum potential density (referenced to 355 the surface) is slightly larger than 1027.87 kg/m³ (Fig. 1(c-d)). We therefore take ρ_d = 356 $1027.88 \, kg/m^3$ as the upper interface, $z = \eta(x, y, t)$, of the dense water layer. To 357 examine the drivers of the cross-slope transport, we write the downslope transport term (i.e. 358 the Coriolis force) on the left-hand side, and consider all other (right-hand-side) terms to 359 360 be drivers,

361
$$\underbrace{\int_{-H}^{\eta} v dz}_{transport} = \underbrace{\frac{1}{f} \int_{-H}^{\eta} \frac{\partial u}{\partial t} dz}_{acceleration} + \underbrace{\frac{1}{f} \int_{-H}^{\eta} \mathbf{u} \cdot \nabla u dz}_{advection} + \underbrace{\frac{1}{f \rho_0} \int_{-H}^{\eta} \frac{\partial p}{\partial x} dz}_{pressure\ gradient} - \underbrace{\frac{1}{f \rho_0} \int_{-H}^{\eta} \frac{\partial \tau^x}{\partial z} dz}_{friction}.$$
(7)

Averaged over several TRWs cycles, the acceleration term is relatively small in our model results, so we omit this term. Neglecting this term and averaging Eq. (7) in time yields

364
$$\underbrace{\int_{-H}^{\eta} v dz}_{transport} \approx \underbrace{\frac{1}{f} \int_{-H}^{\eta} \mathbf{u} \cdot \nabla u dz}_{advection} + \underbrace{\frac{1}{f \rho_0} \int_{-H}^{\eta} \frac{\partial p}{\partial x} dz}_{pressure\ gradient} - \underbrace{\frac{1}{f \rho_0} \int_{-H}^{\eta} \frac{\partial \tau^x}{\partial z} dz}_{friction}, \quad (8)$$

where the overbar indicates time average over ~5 TRW periods. To describe the distribution of dense water on the continental slope more conveniently, we define the region shallower than 1300m isobath as the upper slope, and the depth range 1300m-1900m as the mid-slope, and deeper than 1900m as the lower slope.

4.1.1 Downslope Ekman transport in steady overflows

365

366

367

368

369

370

371

372

We first discuss the zonal momentum balance for our steep slope case, which is plotted in Fig. 7. The dense overflow exits the trough and descends the continental slope relatively rapidly, reaching the \sim 1900m isobath by $x\sim$ 380 km. During this phase of the

descent, the flow undergoes a geostrophic adjustment process, with both friction and advection supporting the down-slope transport. The pressure gradient force (Fig. 7b) plays a secondary role. After geostrophic adjustment, the dense water flows approximately along isobaths, with a relatively gradual descent down the slope (Fig. 2b). During this phase of the descent, the advection term becomes negative, partially opposing the tendency of the bottom friction to drive the downslope transport. Time series of the zonally-integrated (along the blue dashed line in Fig. 7(a-d)) downslope transport show that periodic fluctuations due to TRWs still exist in this simulation, with a period of ~21h (Fig. 7e). However, this signal is weak compared with the time-mean, and thus does not contribute to the transport significantly. Thus in this parameter regime the dense overflow moves westward along isobaths approximately at the Nof speed (U_N), and is pushed down-slope by the frictional bottom Ekman transport. The frictional down-slope transport is partially offset by advection, i.e. the relative vorticity is negative (Fig. 2(a, b)), which increases the magnitude of the absolute vorticity, and thus decreases the generalized Ekman transport (Wenegrat et al. 2017).

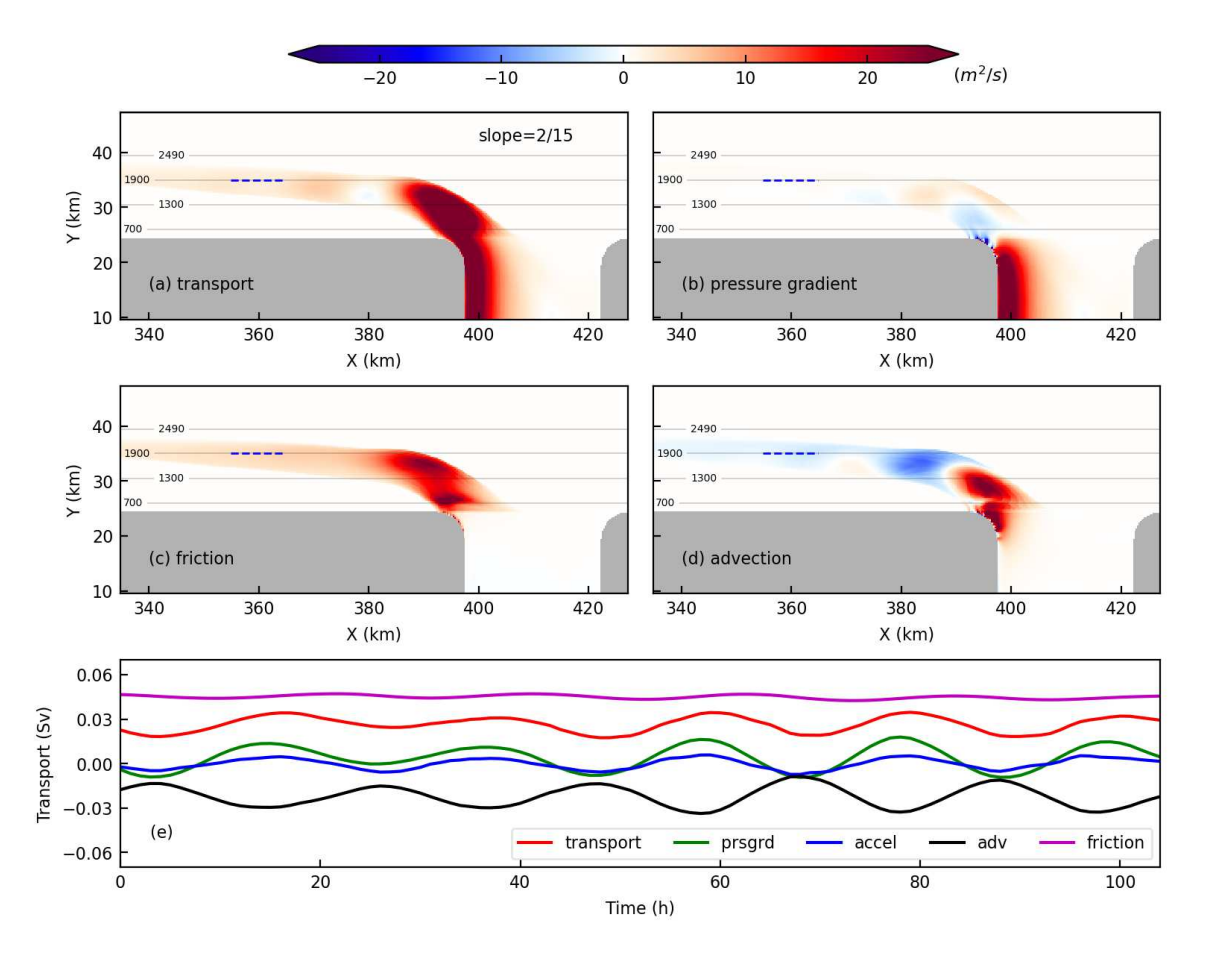


Figure 7. Dense overflow layer momentum budget in the steep slope case. (a-d) Time averaged and vertical integrated downslope transport, and the pressure gradient, friction and advection terms defined in Equation (8), respectively. Contours indicate bathymetry, and the dashed blue line is the section (10km wide) used to diagnose the time series of zonally-integrated downslope transport. (e) Time series of the zonally and vertically integrated momentum balance. Note, in panel (e) we include the acceleration term to show the complete momentum balance.

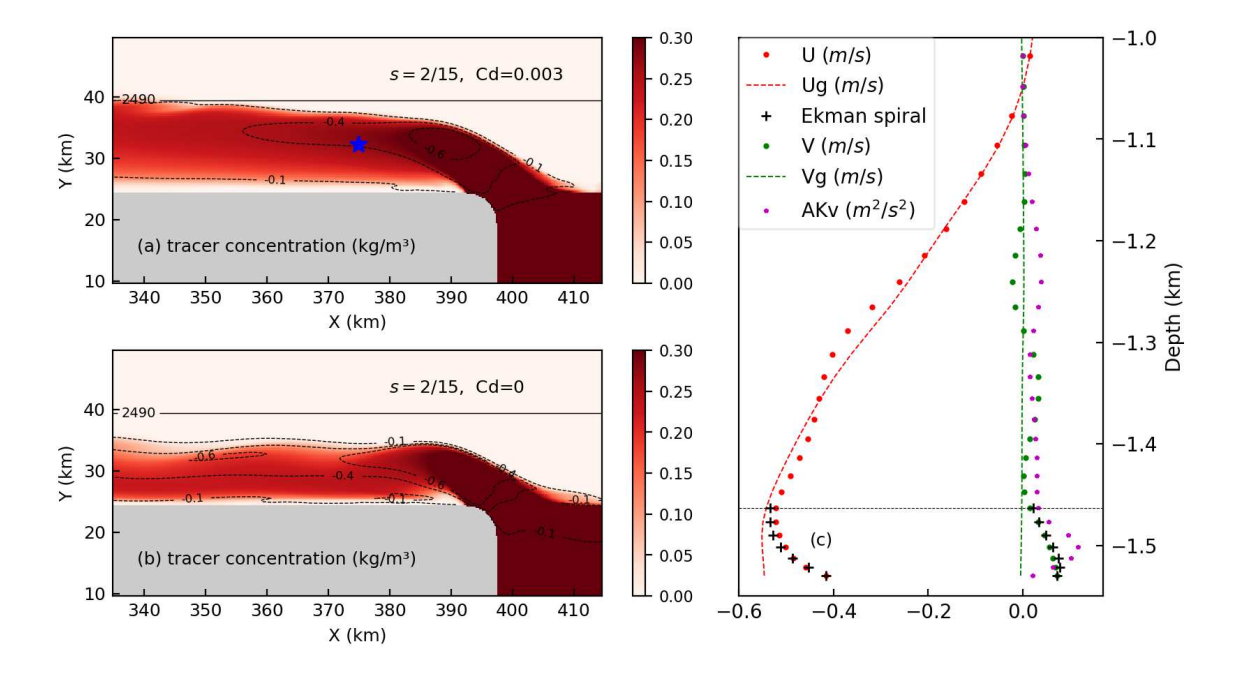


Figure 8. (a) Snapshot of bottom tracer concentration with bottom friction coefficient of Cd=0.003. Contours (dashed line) indicate along-slope velocity, and the solid line (2490) indicates the bottom of the continental slope. (b) Bottom tracer concentration with zero bottom friction. Other symbols are the same as in panel (a). (c) Vertical structure of the horizontal velocity and the eddy viscosity coefficient at the location shown by blue star in panel (a). The black dashed line indicates the vertical level at which we obtain u_q , v_q .

To isolate the effect of bottom friction experimentally, we conduct a comparative experiment with zero bottom friction (Cd=0) for the steep slope. In this comparative experiment, we also use a passive tracer to track the dense overflow. The results show that the dense overflow exhibits approximately no descent if the bottom friction is zero (Fig. 8b). We further analyze the vertical structure of horizontal velocity to check whether it is structured as a bottom Ekman spiral. The theoretical bottom Ekman spiral (Vallis, 2019) can be expressed as

411
$$u(z) = u_g + A_0 e^{-\frac{z}{d}} \cos\left(\frac{z}{d}\right) - B_0 e^{-\frac{z}{d}} \sin\left(\frac{z}{d}\right), \quad (9)$$

412
$$v(z) = v_g + B_0 e^{-\frac{z}{d}} \cos\left(\frac{z}{d}\right) + A_0 e^{-\frac{z}{d}} \sin\left(\frac{z}{d}\right), \quad (10)$$

where $A_0 = (u_b - u_g)$, $B_0 = (v_b - v_g)$, $d = \sqrt{\frac{2A_z}{f}}$, u_b and v_b are the components of the 413 bottom velocity, u_g and v_g are the components of the interior geostrophic velocity, A_z is 414 the vertical viscosity, and z is the height above bottom. To construct the theoretical Ekman 415 spiral, we take the bottom boundary velocity components u_h and v_h directly from the 416 model output, and the interior geostrophic velocity components u_g and v_g are taken from 417 the seventh grid level (~80mab), below which the eddy viscosity increases substantially 418 (Fig. 8c). The eddy viscosity A_z is estimated by averaging over the bottom seven levels. 419 The predicted Ekman spiral is very close to the velocities diagnosed from the model output, 420 as shown in Fig. 8c. This supports the conclusion that the downslope flow can be 421 understood as a bottom Ekman transport. 422

4.1.2 TRWs accelerate the descent of dense water

423

424

425

426

427

When the slopes are moderate or small ($s \leq 0.1$), TRWs occur and produce cross-slope velocities that are comparable to the along-slope velocity (Fig. 2(d, f)). This cross-slope velocity is able to bring dense water down the slope efficiently, suggesting that may play an important role in the descent of dense water.

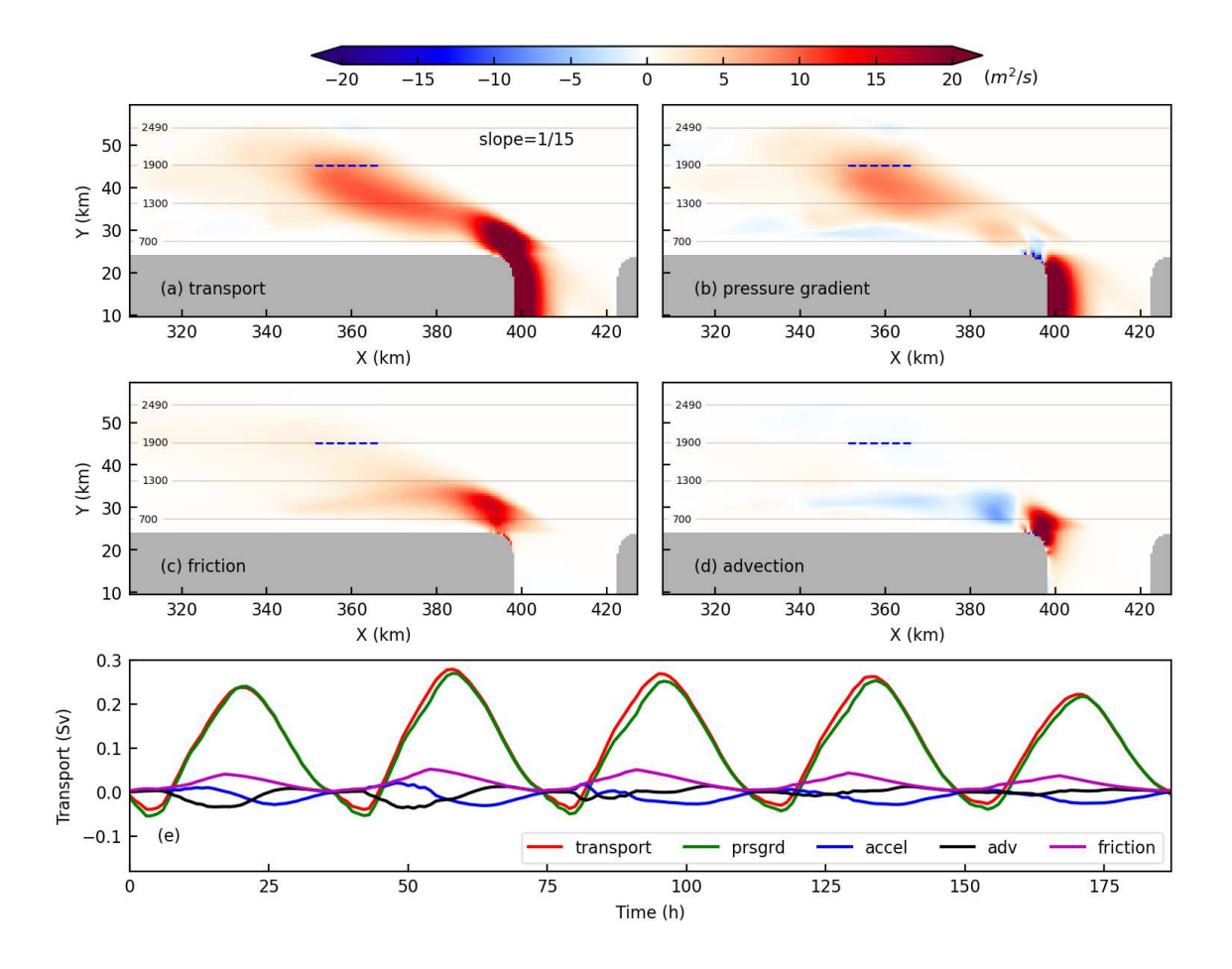


Figure 9. Dense overflow layer momentum budget for the moderate slope case. (a-d) Time-averaged and vertically-integrated downslope transport, and pressure gradient, friction and advection terms defined in Equation (8), respectively. Contours indicate bathymetry, and the dashed blue line is the section (15km wide) used to diagnose the time series of the zonally-integrated downslope transport. (e) Time series of the zonally and vertically integrated momentum balance.

We first examine the dense overflow momentum budget for the moderate slope experiment (Fig. 9). The results show that the pressure gradient force (Fig. 9b), friction (Fig. 9c) and advection (Fig. 9d) terms all make significant contributions to the downslope transport. During geostrophic adjustment (i.e. upper slope), advection and friction terms dominate the zonal momentum balance, but these contributions are negligible by the time the overflow reaches the 1300m isobath. Beyond this, the transport is dominated by the pressure gradient force (Fig. 9b). Fig. 9e shows that the downslope transport induced by the pressure gradient exhibits significant temporal fluctuations, with a periodicity that is consistent with TRWs (~38h). This indicates that the down-slope transport occurs due to

the rectified effect of zonal pressure gradient forces imparted by passing TRWs, and supports our energetics-based argument (see section 1) that the genesis of TRWs transports dense water down-slope.

The force exerted by the horizontal pressure gradient on an abyssal isopycnal layer can be rewritten in terms of the interfacial form stress (IFS) across the isopycnal interface, which has been identified as the agent of eddy-induced down-slope flows in previous studies (Stewart and Thompson 2016; Morrison et al. 2020). To connect our findings with previous studies, we note that the vertical integrated pressure gradient force can be rewritten as

452
$$\frac{1}{f\rho_0} \langle \int_{-H}^{\eta} \frac{\partial p}{\partial x} dz \rangle = -\frac{1}{f\rho_0} \underbrace{\langle p_{\eta} \frac{\partial \eta}{\partial x} \rangle}_{IFS} + \frac{1}{f\rho_0} \left[\int_{-H}^{\eta} p dz \right], \quad (11)$$

where $z=\eta$ is the elevation of the isopycnal interface, p_{η} denotes the pressure on the isopycnal interface, the angle brackets indicate a zonal integral, and the square brackets denote the difference between the end-points of the zonal integral. The first term on the right-hand side of (11) is proportional to the IFS (see e.g. Vallis (2019)); the second term vanishes when the integral is taken over a zonal range that entirely spans the dense water layer, i.e. when $\eta=-H$ at the end-points of the zonal integration. Thus the down-slope transport can approximately be understood as the result of transient IFS that transfers zonal momentum downward into the DSW layer. This mechanism is a consequence of the formation of TRWs, whether or not the growth of these TRWs leads to the formation of nonlinear eddies.

The dynamics of down-slope transport in the small slope (s = 1/30) experiment are similar to those of the moderate slope experiment. As shown in Fig. 10, the downslope transport is again dominated by horizontal pressure gradient term (Fig. 10b) and varies at the frequency of the TRWs (Fig. 10e), while the roles of bottom Ekman transport (Fig. 10c) and advection (Fig. 10d) are secondary.

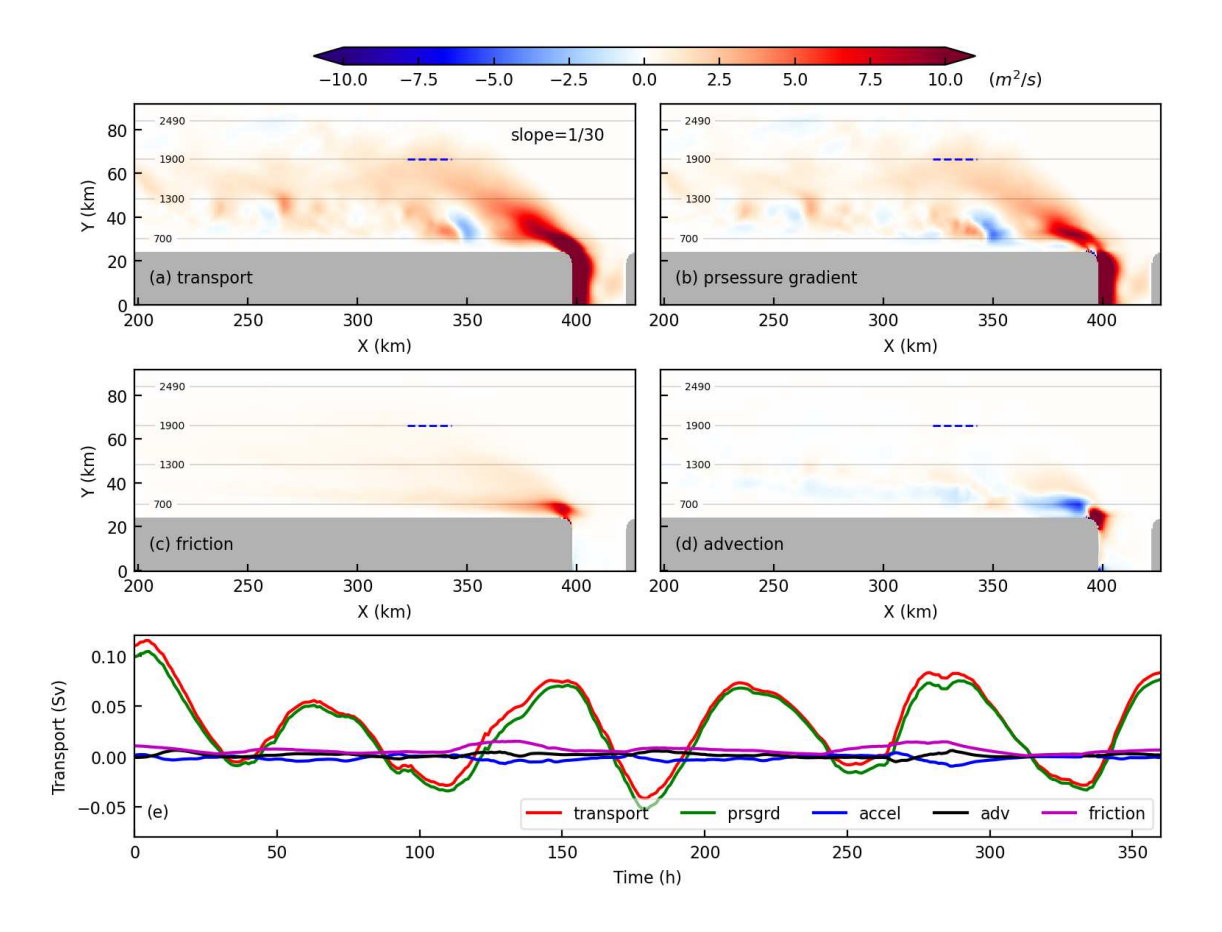


Figure 10. Dense overflow layer momentum budget in our small slope case. (a-d) Time-averaged and vertically-integrated downslope transport, and pressure gradient, friction and advection terms in Equation (8), respectively. Contours indicate bathymetry, and the dashed blue line is the section (20km wide) used to diagnose time series of the zonally-integrated downslope transport; (e) Time series of the zonally and vertically integrated momentum balance.

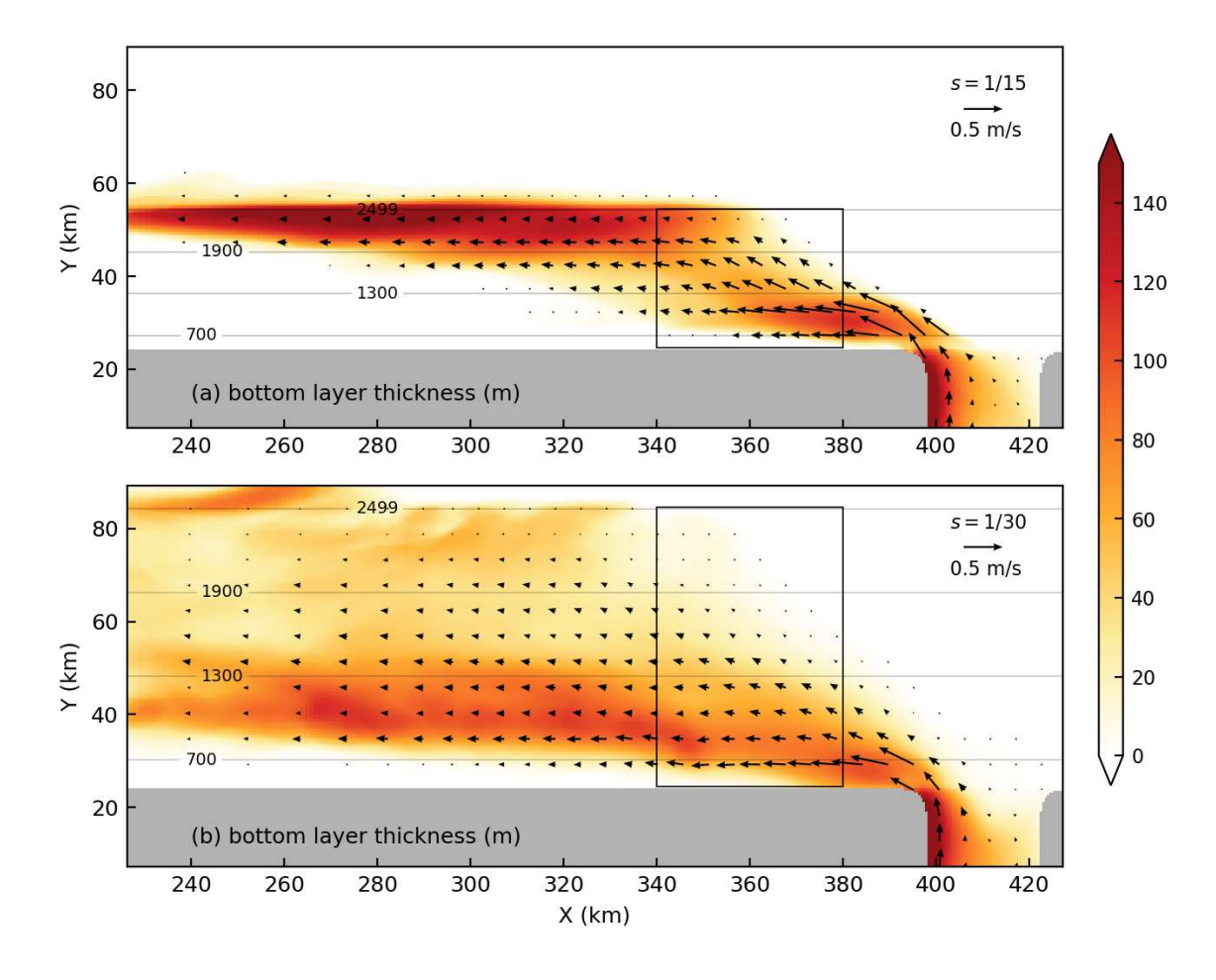


Figure 11. Time averaged (over 5 TRW periods) dense overflow layer thickness. The arrows indicate time- and vertically averaged flow in the dense overflow layer. Contours indicate bathymetry, and the black rectangles represent the area used in Fig. 12. (a) Moderate slope experiment (s = 1/15); (b) Small slope experiment (s = 1/30).

4.2 Descent rate over different overflow regimes

Although the mechanism underlying the down-slope transport is similar in the moderate slope and small slope cases, the time-averaged dense water distribution (Fig. 11) shows that the efficiency with which DSW descends the slope is quite different. As shown in Fig. 11a, the dense overflow descends relatively quickly in the moderate slope case, reaching the bottom of the slope at about 50km downstream of the trough. However, in the small slope case, most of the dense water is confined to the upper slope, and the overflow is spread along the slope over a distance of hundreds of km (Fig. 11b). This suggests that the formation of isolated bottom eddies suppresses the descent of DSW for small slopes.

We now quantify how the descent of DSW is influenced by the steepness of the continental slope, and thus by the mechanism of down-slope transport. We define a descent angle (β) as the angle between the pathway of dense water and the isobaths, which is equivalent to the ratio between down-slope and along-slope tracer transport

492
$$tan\beta = \frac{ \iint_{-H}^{\eta} v_d \cdot \tau dz dy dx}{ \iint_{-H}^{\eta} u_d \cdot \tau dz dy dx}.$$
 (12)

Here u_d and v_d are diagnosed components of the velocity, averaged vertically over the dense overflow layer, and the area integral $\oiint(\cdot)dxdy$ is taken over the region of most rapid descent $(340km \le x \le 380km)$, as indicated by the black rectangles in Fig. 11. Note, the selected regions are downstream of x = 380km to avoid the influence of the initial geostrophic adjustment. The results are shown in Fig. 12, which shows that the diagnosed descent angle is small for the steep slope case $(s \ge 0.1)$, and increases quickly for moderate slopes (0.05 < s < 0.1), but suddenly drops for smaller slopes $(s \le 0.05)$. Based on the transition of diagnosed descent angle, we roughly divide them into steady, wavy and eddying regimes as shown in Fig. 12.

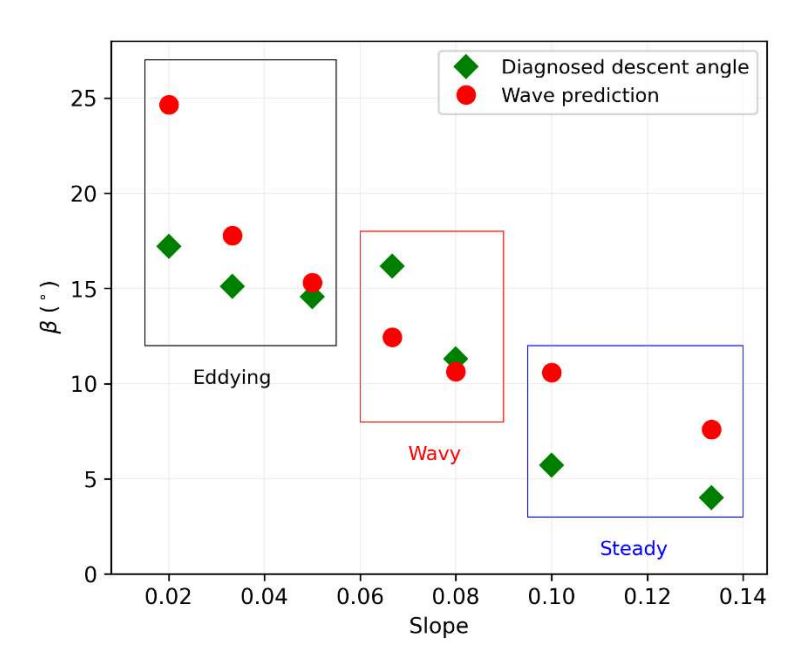


Figure 12. Diagnosed (green diamonds) and predicted (red dots, Equation (16)) descent angle of the tracers on the continental slope and in the zonal range of $340km \le x \le 380km$, as shown by the black rectangles in Fig. 11. The black, red and blue rectangles delineate eddying, wavy and steady overflow regimes, respectively.

To explain this, we formulate a simplified theoretical predication based on potential vorticity (PV) conservation. As noted above, the TRWs are induced by the squeezing of overlying water. The isopycnal PV may be written as

$$PV = \frac{f + \zeta}{H}, \tag{13}$$

- here H is the thickness of the overlying water. The change of relative vorticity depends on
- the compression as pulses of dense water pass by, and can be expressed as

$$\zeta = -\frac{h}{H}f, \qquad (14)$$

- where h is the thickness of dense overflow (see Fig. 3). The magnitude of circulation
- velocity (v_e) can then be scaled as

504

505

506507

508

509

$$v_e = \frac{fhL}{H} = \frac{fh\lambda}{4H}.$$
 (15)

- Here, we use a quarter of predicted wavelength (λ , Fig. 6) by Equation (5) as the spatial
- scale L, see Swaters and Flierl (1991) for details. As noted above, the dense water and
- 520 TRWs move westward together (Fig. 5), which means the dense water will be carried
- downslope continuously by the offshore circulation of TRWs as it flows westward (Fig. 2d
- and Fig. 3). Assuming that the dense overflow is advected down-slope by the circulation
- velocity v_e , we predict a descent angle that is appropriate for the wavy regime,

$$tan\beta = \frac{v_e}{U_N} = \frac{f^2h\lambda}{4Hg's}.$$
 (16)

- However, the dynamics actually transit through steady, wavy and eddying regimes as the
- topographic slope varies (Figs. 2 and 12). Therefore, while Equation (16) should be
- 527 appropriate for wavy regime, we anticipate it over-estimating the descent angle in the
- steady and eddying regimes, in which we expect the descent of DSW to be suppressed. In

addition, Equation (16) is a very rough estimate: it depends on the choice of isopycnal to define dense water (thus h), and the circulation velocity is derived from isopycnal PV conservation (Equation (13)), while the TRWs are bottom intensified in stratified environments (Pedlosky, 1987). Therefore, as shown in Fig. 12, Eq. (16) does not quantitatively agree with the diagnosed descent angle, but does capture the trend qualitatively. The physical explanation for this trend is that as the slope steepness decrease, the Nof speed decreases nearly linearly (Fig. 5a), while the strength of TRWs does not change significantly, thus the descent angle increases.

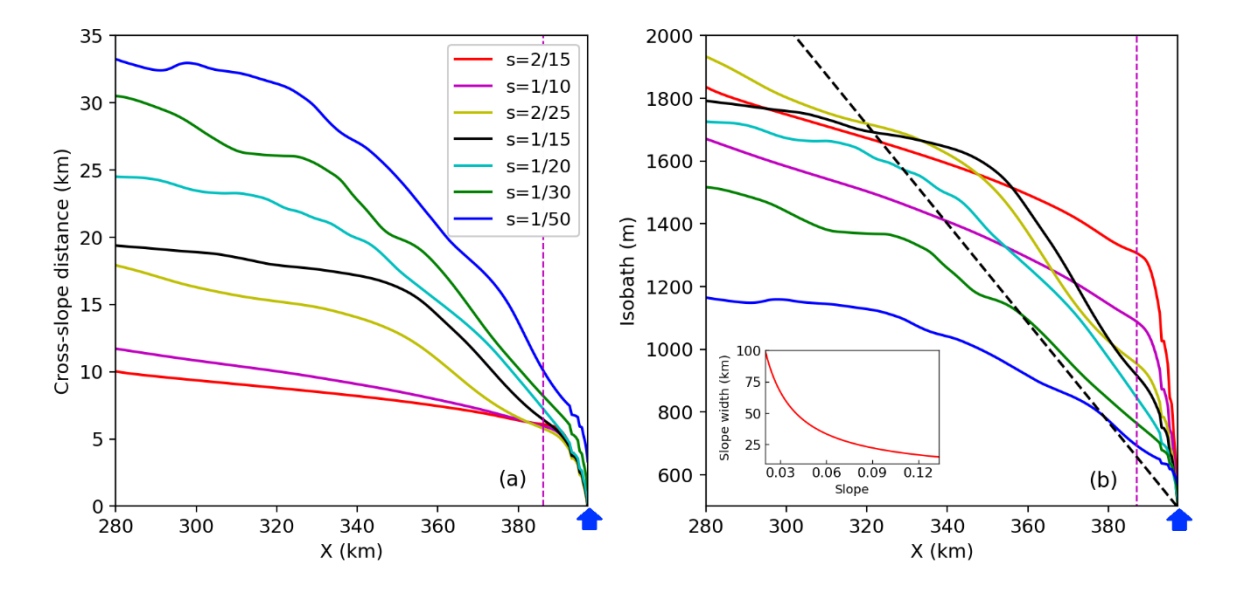


Figure 13. (a) Pathway of the cross-slope tracer centroid for varying slope steepnesses. (b) As (a), but using isobaths as the meridional coordinate. The inset shows the continental slope width with varying slope steepness. The magenta dashed line approximately indicates the location where the dense overflows complete the initial geostrophic adjustment. The black dashed line indicates the descent angle in the x-z plane predicted by Equation (19).

As noted above, both steep slopes and small slopes lead to suppression of down-slope transport, via formation of a steady, frictional-geostrophic flow and via formation of coherent eddies over the upper slope, respectively. This suggests that moderate slopes should lead to the most efficient export of DSW. To test this, we use the time-averaged center of mass of the of passive tracer field to identify the pathway of the dense water overflow:

$$y_{\tau}(x) = \frac{\overline{\int_{0}^{\infty} \int_{-H}^{0} y \cdot \tau dz \, dy'}}{\overline{\int_{0}^{\infty} \int_{-H}^{0} \tau dz dy}}.$$
 (17)

In absolute terms, the tracer centroid exhibits a monotonic increase in the rate at which it descends the continental slope, as shown in Fig. 13a. However, switching to isobaths as a meridional coordinate (Fig. 13b) reveals that the rate at which the tracer reaches the deep ocean varies non-monotonically with the slope steepness. Despite the increasing continental slope width (see inset in Fig. 13b) as the slope steepness decreases, the tracer pathways in different experiments intersect due to the transition between different overflow regimes. For example, the tracers initially descend quickly in the steep slope experiments ($s \ge 0.1$) during geostrophic adjustment process, but after that the descent rate becomes much slower, and is subsequently overtaken by the moderate slope experiments (0.05 < s < 0.1).

Building on Equation (16), we can obtain a relationship between the rate at which the dense water traverses isobaths versus along-slope distance. The speed at which the dense water traverses isobaths can be directly related to the cross-slope flow via

$$v_z = v_e \cdot s. \tag{18}$$

Then we estimate the descent angle in the x-z plane, γ , as

$$\gamma = \frac{v_z}{U_N} = \frac{f^2 h \lambda}{4Hg'}.$$
 (19)

This descent angle no longer depends on the slope steepness if other parameters are fixed, which may explain why the centroids follow very similar pathways in the wavy regime (Fig. 13b, black and yellow lines). The black dashed line in Fig. 13b show the predicted decent angle for s = 1/15, which is close to the diagnosed pathway.

5 Summary and Discussion

Dense overflows are intrinsically unstable on sloping topography, forcing coupled TRWs which oscillate throughout the water column (Swaters, 1991; Reszka et al., 2002; Guo et al., 2014; Han et al., 2022). It follows from conservation of energy that the dense overflow must descend the slope to release potential energy to energize the oscillations.

However, what determines the properties (e.g. wavelength and frequency) of the overflow-forced TRWs and how these are related with the descent of DSW are still not clear. In this study, we use a series of idealized numerical model experiments (see Section 2) to investigate the properties of overflow-forced TRWs and the associated downslope transport of DSW over varying slope steepness, which approximate different overflow regimes around Antarctic coast.

In Section 3 we showed that motions of DSW pulses and the overlying TRWs are jointly constrained by the dynamics of linear plane TRW theory and by the Nof (1983) geostrophic propagation speed of dense anomalies over a sloping bottom. Specifically, the Nof speed closely predicts the phase speed of the TRWs, which in turn predicts the wavelength and frequency of the TRWs via linear plane wave dynamics (Fig. 6). Although the results are largely based on the assumptions of linear TRW theory and no across-slope phase propagation, these assumptions have been verified through TRW dispersion relationship (Fig. 6) and the orientation of ocean current oscillations (Fig. A1) respectively. These findings build a dynamical connection between dense overflow and the properties of TRWs, and provides a general theoretical prediction of the wavelengths and frequencies of TRWs that should occur in different overflows in nature.

In section 4 we investigated how the dynamics and rate of the DSW descending vary across a range of slope steepnesses, over which the overflow dynamics transit between "steady", "wavy" and "eddying" regimes (see Fig. 12 and Han et al. (2022)). In the steady regime ($s \ge 0.1$), the TRWs are suppressed and the descent of DSW is approximately driven by a bottom Ekman transport that is slightly modified by the time-mean relative vorticity (Fig. 7). In the wavy regime (0.05 < s < 0.1), DSW descends the slope via advection by TRWs, supported by transient interfacial form stress across the top of the DSW layer (Fig. 9). When the slope steepness is relatively small ($s \le 0.05$), these TRWs generate coherent cyclonic eddies that is consist of overlying water column and bottom dense water, and translate along-isobath (Mory et al., 1987; Han et al., 2022). The cyclonic eddies tend to drift upslope under the influence of their own vorticity advection (Mory et al., 1987; Carnevale et al., 1991), hence the tendency for the coherent eddies is to be confined at the top of the slope. The coherent eddies have weak interactions with surrounding ocean and

can be idealized to be isolated systems with no momentum transfer to surrounding fluid (Mory et al., 1987), thus the dense water does not descend downslope from the perspective of energy conservation.

The transitions between different overflow regimes lead to a non-monotonic dependence of the rate at which DSW crosses isobaths, i.e. of the angle of the DSW's descent in the along-slope/depth plane, on the slope steepness (Fig. 13b). In the wavy regime this descent angle can be accurately predicted by assuming that the DSW translates along-slope at the Nof speed, and is advected steadily downslope by the cross-slope velocity anomalies associated with the TRWs, which in turn are predicted by linear plane TRW theory (Figs. 12 and 13b).

The formation of isolated bottom eddies may be linked to the larger interaction parameter (μ) for smaller slope steepness (Fig. 5b). As has been discussed above, larger μ indicates stronger interactions between the dense overflow and the overlying water, which may be strong enough to form the coherent eddies (Mory, 1985; Mory et al., 1987). In contrast, there are also strong nonlinear eddies in the overlying water in moderate slope case (Fig. 2c, Han et al., 2022), while the interaction parameter is smaller due to its larger slope steepness (Fig. 5b), that is probably why there is no isolated bottom eddies formation.

We note that our simulations are rather idealized to simplify the dynamical analysis. For example, some previous studies have identified both topographic steering (Jiang and Garwood, 1998; Darelius and Wahlin, 2007; Matsumura and Hasumi, 2010; Wang et al., 2009) and tidal advection (Whitworth and Orsi, 2006; Padman et al., 2009; Wang et al., 2010; Bowen et al., 2021) as potentially important contributors to the descent of DSW. Further work is required to establish how the presence of tides or asymmetries in the structure of the continental slope might alter the formation of TRWs and the different overflow regimes explored in this study.

We also note some limitations to our methodology: the prescribed dense inflow flux (\sim 0.2Sv) in our simulations is relatively small compared to the rate of DSW export in the Ross Sea (\sim 0.8Sv, Gordon et al., 2009) and the Weddell Sea (\sim 1.6 \pm 0.5Sv, Foldvik et al., 2004). Therefore, caution is required in directly comparing the production of AABW with

in situ observations; here instead we focus on the different dynamical regimes that occur in the overflow as the slope steepness varies. More realistic (e.g. regional) model configurations would be required to assess the similarity between the overflow regimes found in nature with those represented by our model. Additionally, we note that our vertically-integrated momentum budget analysis (see Section 4) uses a relatively large reference density $\rho_d = 1027.88 \, kg/m^3$ to define the upper boundary of the DSW layer, in order to ensure that the diagnostics exclude the overlying waters. This choice tends to amplify the contribution of bottom Ekman transport to the down-slope flow, because the bottom boundary layer occupies a larger fraction of the DSW layer under this definition. However, the Ekman transport contribution remains relatively small in the wavy and eddying regimes, which underscores the importance of TRW-induced interfacial form stresses in these regimes.

In summary, the two key outcomes of this study are: (i) identification of the dynamics underlying the selection of TRW wavelengths and frequencies in dense overflows over continental slopes; and (ii) demonstrating that the transition between frictionally-dominated, TRW-dominated and eddy-dominated downslope flows leads to a non-monotonic dependence of the DSW descent on the slope steepness. These findings offer a potential explanation for the varying frequencies (or absence) of TRWs that have been observed in different oceanic overflows, and for the presence/absence of TRWs or nonlinear eddies arising in these overflows (Jensen et al., 2013; Nakayama et al., 2014; Hopkins et al., 2019; Darelius et al., 2015; Gordon et al., 2009; Williams et al., 2010). Future work will be required to connect the idealized theories for TRW characteristics and DSW descent presented here with in situ observations, potentially with the aid of more comprehensive model configurations that incorporate complexities such as tidal flows and bathymetric ridges.

Acknowledgments

This work is supported by grants from the National Natural Science Foundation of China (41730535). A.L.S. was supported by the National Science Foundation under Grant Numbers OCE-1751386 and OPP-2023244. The authors declare no conflicts of interest.

Data availability

The Matlab scripts for the generation of numerical simulations and the configurations of ROMS are available at: https://doi.org/10.5281/zenodo.6778078.

668 Appendix

The orientation of TRW phase propagation can be indicated by the ocean current ellipse (Muenchow et al., 2020). Here we connect the tail of ocean current vector over 5 TRW periods to show local rotations of wave circulation. As shown in Fig. A1, the principal axis of current oscillations is almost across-slope, which indicates that the phase velocity vector is almost along-slope (Muenchow et al., 2020). Here, we only show the case with s = 1/15, but other experiments with varying slope steepnesses have similar results.

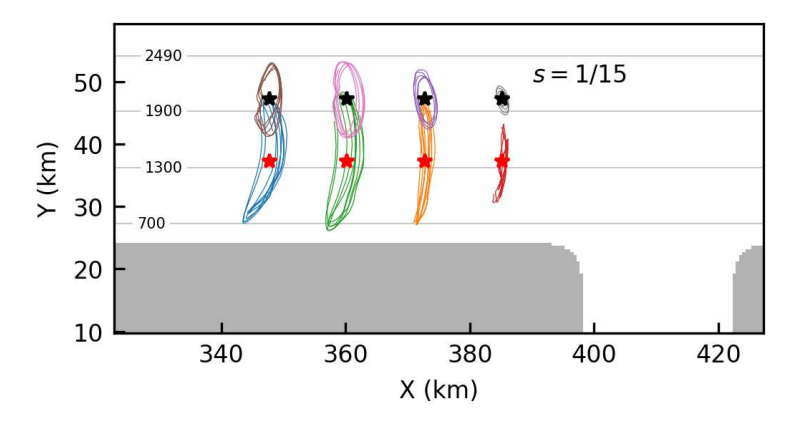


Figure A1. Selected 8 sites (black and red stars) showing ocean current rotations in the 30th σ layer (note that there are 60 layers in total), which is around 880m and 600m above seafloor for the black and red stars, respectively. We connect the tail of flow vector over 5 TRW periods in each site to approximate ocean current ellipse. The flow vector $\mathbf{v} = (u', v')$, where $u' = u - \bar{u}$, $v' = v - \bar{v}$, and the overbar indicate time average over 5 TRW periods. Note the flow vector has been scaled.

683 References

- Von Appen, W. J., Pickart, R. S., Brink, K. H., & Haine, T. W. N. (2014). Water column
- structure and statistics of denmark strait overflow water cyclones. Deep-Sea Research
- 686 Part I: Oceanographic Research Papers, 84, 110–126.
- 687 https://doi.org/10.1016/j.dsr.2013.10.007
- Bowen, M. M., Fernandez, D., Forcen-Vazquez, A., Gordon, A. L., Huber, B., Castagno,
- P., & Falco, P. (2021). The role of tides in bottom water export from the western Ross
- 690 Sea. Scientific Reports, 11(1), 1–11. https://doi.org/10.1038/s41598-021-81793-5
- Daae, K., Fer, I., & Darelius, E. (2019). Variability and mixing of the Filchner overflow
- plume on the continental slope, Weddell sea. Journal of Physical Oceanography, 49(1),
- 693 3–20. https://doi.org/10.1175/JPO-D-18-0093.1
- Darelius, E., & Wåhlin, A. (2007). Downward flow of dense water leaning on a submarine
- ridge. Deep-Sea Research Part I: Oceanographic Research Papers, 54(7), 1173–1188.
- 696 https://doi.org/10.1016/j.dsr.2007.04.007
- Darelius, E., Smedsrud, L. H., Østerhus, S., Foldvik, A., & Gammelsrød, T. (2009).
- Structure and variability of the Filchner overflow plume. Tellus, Series A: Dynamic
- 699 Meteorology and Oceanography, 61(3), 446–464. https://doi.org/10.1111/j.1600-
- 700 0870.2009.00391.x
- 701 Darelius, E., Fer, I., Rasmussen, T., Guo, C., & Larsen, K. M. H. (2015). On the modulation
- of the periodicity of the Faroe Bank Channel overflow instabilities. Ocean
- 703 Science, 11(5), 855-871. https://doi.org/10.5194/os-11-855-2015
- Foldvik, A., Gammelsrød, T., Øterhus, S., Fahrbach, E., Rohardt, G., Schröder, M., et al.
- 705 (2004). Ice shelf water overflow and bottom water formation in the southern Weddell
- 706 Sea. Journal of Geophysical Research: Oceans, 109(2), 1–15.
- 707 https://doi.org/10.1029/2003jc002008
- Gawarkiewicz, G., & Chapman, D. C. (1995). A numerical study of dense water formation
- and transport on a shallow, sloping continental shelf. Journal of Geophysical Research:
- 710 Oceans, 100(C3), 4489-4507. https://doi.org/10.1029/94JC01742

- Gordon, A. L., Orsi, A. H., Muench, R., Huber, B. A., Zambianchi, E., & Visbeck, M.
- 712 (2009). Western Ross Sea continental slope gravity currents. Deep-Sea Research Part
- 713 II: Topical Studies in Oceanography, 56(13–14), 796–817.
- 714 https://doi.org/10.1016/j.dsr2.2008.10.037
- Han, X., Stewart, A. L., Chen, D., Lian, T., Liu, X., & Xie, X. (2022). Topographic Rossby
- 716 wave-modulated oscillations of dense overflows. Journal of Geophysical Research:
- Oceans, 127, e2022JC018702. https://doi.org/10.1029/2022JC018702
- Hopkins, J. E., Holliday, N. P., Rayner, D., Houpert, L., Le Bras, I., Straneo, F., ... & Bacon,
- S. (2019). Transport variability of the Irminger Sea deep western boundary current
- from a mooring array. Journal of Geophysical Research: Oceans, 124(5), 3246-
- 721 3278. https://doi.org/10.1029/2018JC014730
- Howard, E., Hogg, A. M. C., Waterman, S., & Marshall, D. P. (2015). The injection of
- zonal momentum by buoyancy forcing in a Southern Ocean model. Journal of
- Physical Oceanography, 45(1), 259–271. https://doi.org/10.1175/JPO-D-14-0098.1
- 725 Ilicak, M., Legg, S., Adcroft, A., & Hallberg, R. (2011). Dynamics of a dense gravity
- current flowing over a corrugation. Ocean Modelling, 38(1-2), 71-84.
- 727 https://doi.org/10.1016/j.ocemod.2011.02.004
- 728 Isachsen, P. E. (2011). Baroclinic instability and eddy tracer transport across sloping
- bottom topography: How well does a modified Eady model do in primitive equation
- 730 simulations? Ocean Modelling, 39(1–2), 183–199.
- 731 https://doi.org/10.1016/j.ocemod.2010.09.007
- Jiang, L., & Garwood Jr, R. W. (1996). Three-dimensional simulations of overflows on
- continental slopes. Journal of Physical Oceanography, 26(7), 1214-1233.
- 734 https://doi.org/10.1175/1520-0485(1996)026<1214:TDSOOO>2.0.CO;2
- 735 Jiang, L., & Garwood Jr, R. W. (1998). Effects of topographic steering and ambient
- stratification on overflows on continental slopes: A model study. Journal of
- 737 *Geophysical Research: Oceans*, 103(C3), 5459-5476.
- 738 https://doi.org/10.1029/97JC03201

- Jensen, M. F., Fer, I., & Darelius, E. (2013). Low frequency variability on the continental
- slope of the southern Weddell Sea. Journal of Geophysical Research: Oceans, 118(9),
- 741 4256–4272. https://doi.org/10.1002/jgrc.20309
- Johnson, G. C. (2008). Quantifying Antarctic Bottom Water and North Atlantic Deep
- Water volumes. Journal of Geophysical Research: Oceans, 113(5), 1–13.
- 744 https://doi.org/10.1029/2007JC004477
- Killworth, P. D. (2001). On the rate of descent of overflows. Journal of Geophysical
- Research: Oceans, 106(C10), 22267–22275. https://doi.org/10.1029/2000jc000707
- Lane-Serff, G. F., & Baines, P. G. (1998). Eddy formation by dense flows on slopes in a
- rotating fluid. Journal of Fluid Mechanics, 363, 229–252.
- 749 https://doi.org/10.1017/S0022112098001013
- Legg, S., Hallberg, R. W., & Girton, J. B. (2006). Comparison of entrainment in overflows
- simulated by z-coordinate, isopycnal and non-hydrostatic models. Ocean Modelling,
- 752 11(1–2), 69–97. https://doi.org/10.1016/j.ocemod.2004.11.006
- Legg, S., Briegleb, B., Chang, Y., Chassignet, E. P., Danabasoglu, G., Ezer, T., et al. (2009).
- 754 Improving Oceanic Overflow Representation in Climate Models. Bulletin of the
- 755 American Meteorological Society, 90(5), 657–670.
- 756 https://doi.org/10.1175/2008BAMS2667.I
- 757 Marques, G. M., Padman, L., Springer, S. R., Howard, S. L., & Özgökmen, T. M. (2014).
- Topographic vorticity waves forced by Antarctic dense shelf water outflows.
- 759 Geophysical Research Letters, 41(4), 1247–1254.
- 760 https://doi.org/10.1002/2013GL059153
- Masich, J., Mazloff, M. R., & Chereskin, T. K. (2018). Interfacial Form Stress in the
- Southern Ocean State Estimate. Journal of Geophysical Research: Oceans, (1), 3368–
- 763 3385. https://doi.org/10.1029/2018JC013844
- Matsumura, Y., & Hasumi, H. (2010). Modeling ice shelf water overflow and bottom water
- formation in the southern Weddell Sea. Journal of Geophysical Research: Oceans,
- 766 115(10), 1–17. https://doi.org/10.1029/2009JC005841

- 767 Mellor, G. L., & Yamada, T. (1982). Development of a turbulence closure model for
- geophysical fluid problems. Reviews of Geophysics, 20(4), 851–875.
- 769 https://doi.org/10.1029/RG020i004p00851
- 770 Mory, M. (1985). Integral constraints on bottom and surface isolated eddies. *Journal of*
- 771 *physical oceanography*, *15*(11), 1433-1438.
- Mory, M., Stern, M. E., & Griffiths, R. W. (1987). Coherent baroclinic eddies on a sloping
- 5773 bottom. Journal of Fluid Mechanics, 183, 45-62.
- 774 https://doi.org/10.1017/S0022112087002519
- Münchow, A., Schaffer, J., & Kanzow, T. (2020). Ocean circulation connecting fram strait
- to glaciers off Northeast Greenland: mean flows, topographic Rossby waves, and their
- forcing. Journal of Physical Oceanography, 50(2), 509-530.
- 778 https://doi.org/10.1175/JPO-D-19-0085.1
- Nakayama, Y., Ohshima, K. I., Matsumura, Y., Fukamachi, Y., & Hasumi, H. (2014). A
- 780 numerical investigation of formation and variability of Antarctic bottom water off
- Cape Darnley, East Antarctica. Journal of Physical Oceanography, 44(11), 2921–
- 782 2937. https://doi.org/10.1175/JPO-D-14-0069.1
- Nof, D. (1983). The translation of isolated cold eddies on a sloping bottom. Deep Sea
- Research Part A, Oceanographic Research Papers, 30(2), 171–182.
- 785 https://doi.org/10.1016/0198-0149(83)90067-5
- Ohshima, K. I., Fukamachi, Y., Williams, G. D., Nihashi, S., Roquet, F., Kitade, Y., et al.
- 787 (2013). Antarctic Bottom Water production by intense sea-ice formation in the Cape
- 788 Darnley polynya. Nature Geoscience, 6(3), 235–240.
- 789 https://doi.org/10.1038/ngeo1738
- Ou, H. W., Guan, X., & Chen, D. (2009). Tidal effect on the dense water discharge, Part 1:
- Analytical model. Deep-Sea Research Part II: Topical Studies in Oceanography,
- 792 56(13–14), 874–883. https://doi.org/10.1016/j.dsr2.2008.10.031
- Padman, L., Howard, S. L., Orsi, A. H., & Muench, R. D. (2009). Tides of the northwestern
- Ross Sea and their impact on dense outflows of Antarctic Bottom Water. Deep-Sea

- 795 Research Part II: Topical Studies in Oceanography, 56(13–14), 818–834.
- 796 https://doi.org/10.1016/j.dsr2.2008.10.026
- 797 Pedlosky, J. (1987). Geophysical fluid dynamics (Vol. 710). New York: springer.
- 798 Pickart, R. S., & Watts, D. R. (1990). Deep western boundary current variability at Cape
- 799 Hatteras. Journal of Marine Research, 48(4), 765-791. https://
- doi.org/10.1357/002224090784988674
- 801 Rhines, P. (1970). Edge-, bottom-, and Rossby waves in a rotating stratified
- fluid. Geophysical and Astrophysical Fluid Dynamics, 1(3-4), 273-302.
- 803 https://doi.org/10.1080/03091927009365776
- 804 Shchepetkin, A. F., & McWilliams, J. C. (2003). A method for computing horizontal
- pressure-gradient force in an oceanic model with a nonaligned vertical coordinate.
- 806 Journal of Geophysical Research: Oceans, 108(3), 1–34.
- 807 https://doi.org/10.1029/2001jc001047
- 808 Spall, M. A., & Price, J. F. (1998). Mesoscale variability in Denmark strait: The PV outflow
- hypothesis. Journal of Physical Oceanography, 28(8), 1598–1623.
- 810 https://doi.org/10.1175/1520-0485(1998)028<1598;MVIDST>2.0.CO;2
- St-Laurent, P., Klinck, J. M., & Dinniman, M. S. (2013). On the role of coastal troughs in
- the circulation of warm Circumpolar Deep Water on Antarctic shelves. *Journal of*
- Physical Oceanography, 43(1), 51-64. https://doi.org/10.1175/JPO-D-11-0237.1
- Stewart, A. L., & Thompson, A. F. (2016). Eddy generation and jet formation via dense
- water outflows across the Antarctic continental slope. Journal of Physical
- Oceanography, 46(12), 3729–3750. https://doi.org/10.1175/JPO-D-16-0145.1
- Swaters, G. E. (1991). On the baroclinic instability of cold-core coupled density fronts on
- a sloping continental shelf. *Journal of Fluid Mechanics*, 224, 361–382.
- https://doi.org/10.1017/S0022112091001799
- 820 Talley, L. D. (2013). Closure of the global overturning circulation through the Indian,
- 821 Pacific, and southern oceans. Oceanography, 26(1), 80–97.
- 822 https://doi.org/10.5670/oceanog.2013.07

- 823 Vallis, G. K. (2019). Essentials of atmospheric and oceanic dynamics. Cambridge
- 824 University Press.
- Wang, D. P., & Mooers, C. N. (1976). Coastal-trapped waves in a continuously stratified
- ocean. Journal of Physical Oceanography, 6(6), 853-863.
- Wang, Q., Danilov, S., & Schröter, J. (2009). Bottom water formation in the southern
- Weddell Sea and the influence of submarine ridges: Idealized numerical simulations.
- Ocean Modelling, 28(1–3), 50–59. https://doi.org/10.1016/j.ocemod.2008.08.003
- Wang, Q., Danilov, S., Hellmer, H. H., & Schröter, J. (2010). Overflow dynamics and
- bottom water formation in the western Ross Sea: Influence of tides. Journal of
- 832 Geophysical Research: Oceans, 115(10), 1–16.
- https://doi.org/10.1029/2010JC006189
- Wang, Q., Danilov, S., Hellmer, H., Sidorenko, D., Schröter, J., & Jung, T. (2013).
- Enhanced cross-shelf exchange by tides in the western Ross Sea. Geophysical
- Research Letters, 40(21), 5735–5739. https://doi.org/10.1002/2013GL058207
- Wenegrat, J. O., & Thomas, L. N. (2017). Ekman transport in balanced currents with
- 838 curvature. Journal of Physical Oceanography, 47(5), 1189-1203.
- https://doi.org/10.1175/JPO-D-16-0239.1
- Williams, G. D., Bindoff, N. L., Marsland, S. J., & Rintoul, S. R. (2008). Formation and
- export of dense shelf water from the Adélie depression, East Antarctica. Journal of
- Geophysical Research: Oceans, 113(4), 1–12. https://doi.org/10.1029/2007JC004346
- Young, W. R. (2012). An exact thickness-weighted average formulation of the Boussinesq
- equations. Journal of Physical Oceanography, 42(5), 692-707.
- 845 https://doi.org/10.1175/JPO-D-11-0102.1